An optimized CIP-FEM to reduce the pollution errors for the Helmholtz equation on a general unstructured mesh

Buyang Li[a], Yonglin Li[a], Zongze Yang[a]

[a]*Department of Applied Mathematics, The Hong Kong Polytechnic University, Hung Hom, Hong Kong*

Abstract

The continuous interior penalty finite element method (CIP-FEM) has shown promise in reducing pollution errors when numerically simulating the Helmholtz equation with high wave numbers. However, its reliance on structured meshes largely limits its applicability. To address this limitation, this paper presents a novel approach to CIP-FEM on general unstructured meshes. The interior penalty parameters of the CIP-FEM are determined in an offline phase through minimizing the residual obtained by substituting the plane waves into the CIP finite element equation. To enhance accuracy, a quasi-Newton algorithm is employed to correct the penalty parameters and minimize errors of the CIP finite element approximations to the plane waves. The calculated interior penalty parameters can be saved, enabling the online solutions of CIP-FEM to be obtained by reusing these parameters for arbitrary sources during practical computations. Numerical experiments are presented to demonstrate the significant reduction of pollution errors for both linear and higher-order CIP-FEMs on unstructured meshes. Furthermore, the proposed algorithm successfully simulates high-frequency acoustic fields in a three-dimensional vehicle cabin with greatly reduced errors within certain fixed computational time, demonstrating its practical effectiveness in real-world scenarios.

Keywords: Helmholtz equation, high wave number, continuous interior penalty finite element method, unstructured mesh, residual minimization, error minimization

MSC(2020): 65B99, 65N30, 78A40

1. Introduction

This article is concerned with the development of new approach to the continuous interior penalty finite element method (CIP-FEM) for the Helmholtz equation in a bounded domain $\Omega \subset \mathbb{R}^d$, $d = 2, 3$, under the impedance boundary condition, i.e.,

$$-\Delta u - k^2 u = f \quad \text{in } \Omega, \tag{1.1}$$

$$\frac{\partial u}{\partial \mathbf{n}} - \mathbf{i}ku = g \quad \text{on } \Gamma = \partial\Omega, \tag{1.2}$$

where $\mathbf{i} = \sqrt{-1}$ and k are the imaginary unit and the wave number, respectively, and $\mathbf{n}$ is the unit outward normal vector on the boundary Γ. The impedance boundary condition (1.2) can be replaced by other boundary conditions, such as the DtN boundary condition [1,2] and PML boundary condition [3–5]. We are mainly interested in the numerical approximation of the Helmholtz equation in the high-frequency case, i.e., $k \gg 1$, with given source functions $f \in L^2(\Omega)$ and $g \in L^2(\Gamma)$.

Email addresses: buyang.li@polyu.edu.hk (Buyang Li), yonglin.li@polyu.edu.hk (Yonglin Li), zongze.yang@polyu.edu.hk (Zongze Yang)

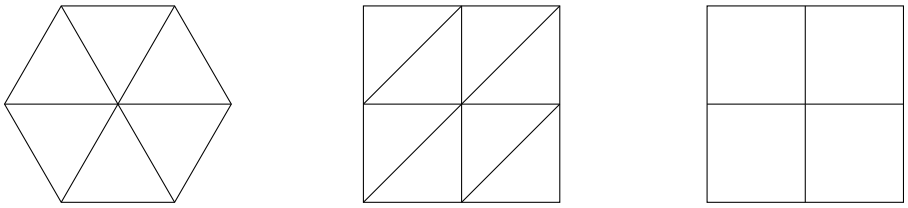

Fig. 1.1: Structured meshes

It is known that the classical FEM for the Helmholtz equation with high wave number suffers from the pollution effect; see [2, 6–12]. For example, the error estimate of the linear FEM is

$$\|u - u_h^{\mathrm{FEM}}\|_{H^1(\Omega)} \leq C_1 kh + C_2 k^3 h^2,$$

provided that k^3h^2 is sufficiently small, where u_h^{FEM} is the classical finite element solution and h is the mesh size. The first term $O(kh)$ in the error bound is of the same order as the interpolation error, and the second term $O(k^3h^2)$ dominates when k^2h is large, which is called the pollution error. The pollution error is not only a technical condition in the error estimates but also observed in the numerical computations. In particular, the mesh condition $h \leq Ck^{-3/2}$ is required to control the pollution error below $O(1)$. This significantly increases the computational cost when k is large. In practice, $h \leq Ck^{-1}$ is acceptable in the practical computation, which requires about $2\pi/C$ degrees of freedom per wave-length and is consistent with the requirement to control the interpolation error. Recently, a variety of FEMs have been developed to reduce the pollution error, including the *hp*-FEM [2, 10, 11, 13, 14], the CIP-FEM [5, 15–21], the discontinuous Galerkin method [22–30], the weak Galerkin method [31–33], the Trefftz methods [34–40], and the multiscale mathods [41–44]. For other approaches to reduce the pollution error for Helmholtz equation, such as the RF-bubble method, GLS-FEM, GFEM, QSFEM, etc., we refer to [9, 10, 45–50].

The CIP-FEM, which was first proposed by Douglas and Dupont [51] for elliptic and parabolic problems in the 1970s, has recently shown great potential in significantly reducing the pollution errors for the Helmholtz equation with high wave number; see [5, 16–18]. The CIP-FEM uses the same approximation space as the FEM but modifies the bilinear form of the FEM by adding a continuous interior penalty term (1.3) at mesh interfaces:

$$J(u,v) = \sum_{e\in\mathcal{E}_h^{\mathrm{I}}} \sum_{j=1}^{p} \gamma_{e,j} h_e^{2j-1} \left\langle \left[\frac{\partial^j u}{\partial \mathbf{n}_e^j}\right], \left[\frac{\partial^j v}{\partial \mathbf{n}_e^j}\right] \right\rangle_e, \tag{1.3}$$

where $\mathcal{E}_h^{\mathrm{I}}$ is the set of all interior edges/faces of the mesh and $\gamma_{e,j}$ denotes the penalty parameters to be determined and may be tuned to greatly reduce the pollution error. The choice of penalty parameter $\gamma = (\gamma_{e,1}, \ldots, \gamma_{e,p})_{e\in\mathcal{E}_h^{\mathrm{I}}}$ is crucial for the CIP-FEM. For some structured meshes, the theoretical parameters can be obtained by the dispersion analysis technique [13]. For example, for equilateral triangulations (see Figure 1.1(a)), the optimal parameters for linear and higher-order CIP-FEMs were derived in [52] and [53], respectively. For isosceles right triangulations (see Figure 1.1(b)), the parameters for linear finite element were derived in [54]. Furthermore, the parameters for arbitrary order tensor-product elements on a Cartesian mesh (see Figure 1.1(c)) were derived in [21].

The key idea of obtaining the optimal penalty parameters by dispersion analysis is to reduce the phase difference, which is represented by $|k - k_h|$, where k_h is the discrete wave number such that $e^{\mathbf{i}k_h \boldsymbol{x}\cdot\boldsymbol{d}}$ solves the homogeneous CIP finite element equation, with $\boldsymbol{d}$ denoting the incident direction of the plane wave. It was shown in [21] that the phase difference could be reduced from $O(k(kh)^{2p})$ to $O(k(kh)^{2p+2})$ by choosing the following theoretical parameter in a tensor-product FEM on a Cartesian

mesh:

$$\gamma_p^{\#} \equiv -\frac{1}{(2p+1)}\left[\frac{p!}{(2p)!}\right]^2. \tag{1.4}$$

The derivation of such optimal penalty parameters requires complex analytical techniques with symbolic operations, and relies heavily on structured meshes.

In practice, the computational domain may not be partitioned into a structured mesh in Figure 1.1. In this case, the optimal penalty parameters cannot be derived by means of the dispersion analysis. The determination of penalty parameters which can effectively reduce the pollution errors of CIP-FEMs on general unstructured meshes still remains open and challenging. In this article, we introduce an innovative approach to numerically determine the penalty parameter in the CIP-FEM. The CIP-FEM that incorporates this new numerical parameter, called an optimized CIP-FEM, shows great ability in reducing the pollution errors on general unstructured meshes. The key idea of determining the numerical penalty parameter is to minimize the error between the plane wave $u_{pw} = e^{\mathbf{i}k\boldsymbol{x}\cdot\boldsymbol{d}}$ and its CIP finite element approximation $u_{pw}^{\mathrm{CIP}}(\gamma; k, \boldsymbol{d})$, i.e.,

$$\gamma^{\mathrm{num}} := \arg\min_{\gamma} \left\| e^{\mathbf{i}k\boldsymbol{x}\cdot\boldsymbol{d}} - u_{pw}^{\mathrm{CIP}}(\gamma; k, \boldsymbol{d}) \right\|. \tag{1.5}$$

Here, $\|\cdot\|$ represents a norm applied to functions, such as the L^2-norm or H^1-norm. The more detailed definitions are given in Sections 3 and 4. In the dispersion analysis for structured meshes, u_{pw}^{CIP} is simply the plane wave function $e^{\mathbf{i}k_h\boldsymbol{x}\cdot\boldsymbol{d}}$ with a discrete wave number k_h. The numerical experiments conducted in this study demonstrate the remarkable ability of the proposed optimized CIP-FEM to effectively reduce pollution errors on general unstructured meshes, where deriving the theoretically optimal penalty parameter through dispersion analysis is not feasible. Notably, the last set of numerical examples involves simulating high-frequency acoustic fields within a vehicle cabin characterized by a complex geometry that cannot be partitioned into structured meshes. The numerical results obtained for this specific application highlight the immense potential of our proposed method.

We would like to emphasize that the computation of the optimization problem (1.5) takes place in an offline phase, in other words, this step should be considered as a one-time preprocessing step. Once the offline computations are finished, the resulting parameter γ^{num} can then be reused in CIP-FEM to obtain an approximated solution of the Helmholtz problem, which is called an online step. Online steps are fast and efficient when the parameter is effective, enabling their repeated execution for Helmholtz problems with different sources and at frequencies smaller than k. Generally, the cost of the offline phase is more expensive than an online step, but fortunately, it only needs to be computed once. We strike a delicate balance, accepting a slight reduction in offline efficiency in exchange for improved online performance. This preference for online efficiency proves advantageous when a substantial number of online computations are required.

The rest of this article is organized as follows. Section 2 provides the definition of CIP-FEM for the Helmholtz equation. Section 3 introduces an optimized CIP-FEM approach utilizing the residual-minimization technique, primarily aimed at reducing pollution errors in linear finite element approximations. In Section 4, a quasi-Newton iteration algorithm is presented to enhance the performance of the optimized CIP-FEM. The numerical experiments are detailed in Section 5, followed by concluding remarks in Section 6.

Throughout the paper, the standard Sobolev spaces, norms, and inner products associated with Helmholtz equations are adopted. For any domain $G \subset \mathbb{R}^d$ and boundary $\Sigma \subset \partial G$, we denote by $(\cdot,\cdot)_G$ and $\langle\cdot,\cdot\rangle_\Sigma$ the inner products on the complex-valued Hilbert spaces $L^2(G)$ and $L^2(\Sigma)$, respectively. In particular, we denote $(\cdot,\cdot) := (\cdot,\cdot)_\Omega$ and $\langle\cdot,\cdot\rangle := \langle\cdot,\cdot\rangle_\Gamma$.

2. The CIP-FEM in online step

Let $\mathcal{T}_h$ be a partition (triangular, tetrahedral, quadrilateral, etc.) of the computational domain Ω. We denote by $h_K = \mathrm{diam}(K)$ the diameter of an element $K \in \mathcal{T}_h$, and denote by $h_e = \mathrm{diam}(e)$ the diameter of any edge/face e on ∂K. The mesh size of the partition is denoted by $h = \max_{K\in\mathcal{T}_h} h_K$. The finite element space of order $p \geq 1$ is defined by

$$V_h := \{v_h \in H^1(\Omega) : v_h|_K \in \mathcal{P}_p(K) \ \text{ for all } \ K \in \mathcal{T}_h\}, \tag{2.1}$$

where $\mathcal{P}_p(K)$ denotes the set of all polynomials on K with degree $\leq p$. For any $u, v \in H^1(\Omega)$, we denote

$$\begin{aligned} a_0(u,v) &:= (\nabla u, \nabla v) - k^2(u,v) - \mathbf{i}k\,\langle u, v\rangle\,, \\ a(u,v) &:= a_0(u,v) + J(u,v), \end{aligned} \tag{2.2}$$

where the penalty term $J(u,v)$ is defined in (1.3). The CIP-FEM for the Helmholtz equation (1.1)–(1.2) reads: Find $u_h \in V_h$ such that

$$a(u_h, v_h) = (f, v_h) + \langle g, v_h\rangle \quad \forall\, v_h \in V_h. \tag{2.3}$$

Let $\{\phi_i\}_{i=1}^N$ be the basis of V_h, where N denotes the number of degrees of freedom. We define the finite element matrix $\mathbf{A}_0$ and the penalty matrix $\mathbf{J} = \mathbf{J}(\gamma)$ by

$$(\mathbf{A}_0)_{il} = a_0(\phi_l, \phi_i) \quad \text{and} \quad \mathbf{J}_{il} = J(\phi_l, \phi_i) \quad \text{for } 1 \leq i, l \leq N, \tag{2.4}$$

and denote the CIP finite element matrix by

$$\mathbf{A}(\gamma) = \mathbf{A}_0 + \mathbf{J}(\gamma).$$

Moreover, we denote by $\mathbf{F} = \mathbf{F}(f, g)$ the N-dimensional vector with the following components:

$$\mathbf{F}_i = (f, \phi_i) + \langle g, \phi_i\rangle\,. \tag{2.5}$$

Therefore, the CIP-FEM (2.3) is equivalent to the following system of linear equations:

$$\mathbf{A}(\gamma)\mathbf{U} = \mathbf{F}, \tag{2.6}$$

with $u_h = \sum_{i=1}^N \mathbf{U}_i \phi_i$.

In the case $\gamma \equiv 0$, the CIP-FEM reduces to FEM, which is equivalent to $\mathbf{A}_0\mathbf{U} = \mathbf{F}$.

3. Residual-minimization approach for the penalty parameters

In this section, we present an algorithm to determine the penalty parameters of CIP-FEM through minimizing the residual in the CIP finite element equations for plane waves in the offline phase. The algorithm is mainly designed for the piecewise linear CIP-FEM (in the case $p = 1$) for reducing the pollution errors in the numerical solution of the Helmholtz equation. It can also be used as a preparation stage for the optimization algorithm proposed in the next section.

For each $e \in \mathcal{E}_h^{\mathrm{I}}$, the penalty parameter $\gamma|_e = (\gamma_{e,1}, \cdots, \gamma_{e,p})^{\mathrm{T}}$ is a p-dimensional vector-valued function. Therefore, the penalty parameter is an element of the following discrete trace space:

$$W_h := \{w_h : w_h|_e \in \mathcal{P}_0(e)^p \cap \mathbb{R}^p \ \text{ for all } e \in \mathcal{E}_h^{\mathrm{I}}\}. \tag{3.1}$$

Here we assume that the penalty parameter is real-valued since the theoretical optimal parameters are always real-valued. We denote the plane wave function by $u_{pw} = e^{\mathbf{i}k\boldsymbol{x}\cdot\boldsymbol{d}}$ with direction $\boldsymbol{d}$. It is easy to

see that u_{pw} is the solution of Helmholtz equation in (1.1)–(1.2) with the following source functions:

$$f_{pw} = 0 \quad \text{in } \Omega \quad \text{and} \quad g_{pw} = \mathbf{i}ke^{\mathbf{i}k\boldsymbol{x}\cdot\boldsymbol{d}}(\boldsymbol{d}\cdot\mathbf{n} - 1) \quad \text{on } \partial\Omega. \tag{3.2}$$

Let I_h be the standard finite element interpolation operator and $\mathbf{U}_{pw}$ be the vector generated by the degrees of freedom of $I_h u_{pw}$, i.e.,

$$I_h u_{pw} = \sum_{i=1}^{N} (\mathbf{U}_{pw})_i \phi_i. \tag{3.3}$$

Inspired by the dispersion analysis, the error of $\mathbf{U}_{pw}$ and the solution $\mathbf{U}$ to (2.6) should be as small as possible. Therefore, a simple way to find a reasonable parameter is to minimize the residual

$$r(\boldsymbol{d}) = \min_{\gamma \in W_h} \|\mathbf{A}(\gamma)\mathbf{U}_{pw} - \mathbf{F}_{pw}\|_K \quad \text{with} \quad \mathbf{F}_{pw} = \mathbf{F}_{pw}(\boldsymbol{d}) := \mathbf{F}(f_{pw}, g_{pw}), \tag{3.4}$$

where K is a real symmetric positive definite matrix and $\|\cdot\|_K$ is the vector norm defined by

$$\|\mathbf{v}\|_K := \sqrt{\mathbf{v}^{\mathrm{H}} K \mathbf{v}}.$$

The matrix K is usually chosen as the identity matrix (refer to the l^2 norm), the mass matrix (refer to the L^2 norm), or the sum of mass matrix and stiffness matrix (refer to the H^1 norm). By the definition of $\mathbf{A}(\gamma)$, it is easy to see that

$$\mathbf{A}(\gamma)\mathbf{U}_{pw} - \mathbf{F}_{pw} = \mathbf{J}(\gamma)\mathbf{U}_{pw} - \mathbf{b}, \tag{3.5}$$

where $\mathbf{b} = \mathbf{b}(\boldsymbol{d}) := \mathbf{F}_{pw} - \mathbf{A}_0\mathbf{U}_{pw}$. From the definition of $\mathbf{J}$ in (1.3) and the definition of $I_h u_{pw}$ in (3.3) we know that $\mathbf{J}(\gamma)\mathbf{U}_{pw}$ is a vector assembled by term $J(I_h u_{pw}, \cdot)$, i.e.,

$$(\mathbf{J}(\gamma)\mathbf{U}_{pw})_l = \sum_{i=1}^{N} \mathbf{J}_{li}(\mathbf{U}_{pw})_i = \sum_{i=1}^{N} J(\phi_i, \phi_l)(\mathbf{U}_{pw})_i = J(I_h u_{pw}, \phi_l), \quad l = 1, 2, \cdots, N.$$

For a given function u, we define the sesquilinear form $\tilde{J}(u) : W_h \times V_h \to \mathbb{C}$ by

$$\tilde{J}(u; w_h, v_h) = \sum_{e \in \mathcal{E}_h^{\mathrm{I}}} \sum_{j=1}^{p} (w_h|_e)_j h_e^{2j-1} \left\langle \left[\frac{\partial^j u}{\partial \mathbf{n}_e^j}\right], \left[\frac{\partial^j v_h}{\partial \mathbf{n}_e^j}\right] \right\rangle_e \quad \forall\, w_h \in W_h,\ v_h \in V_h, \tag{3.6}$$

where $(w_h|_e)_j$ denotes the j-th component of w_h on edge e. Let $\{\psi_i\}_{i=1}^M$ be the basis of W_h and denote

$$\gamma = \sum_{i=1}^{M} \boldsymbol{\gamma}_i \psi_i \in W_h \quad \text{and} \quad \boldsymbol{\gamma} = (\boldsymbol{\gamma}_1, \boldsymbol{\gamma}_2, \cdots, \boldsymbol{\gamma}_M)^{\mathrm{T}}.$$

Furthermore, we denote the $N \times M$ matrix $\tilde{\mathbf{J}}(u)$ by

$$\tilde{\mathbf{J}}(u)_{il} = \tilde{J}(I_h u; \psi_l, \phi_i) \quad \text{for } 1 \le i \le N,\ 1 \le l \le M. \tag{3.7}$$

Then we have

$$\mathbf{J}(\gamma)\mathbf{U}_{pw} = \tilde{\mathbf{J}}(u_{pw})\boldsymbol{\gamma}. \tag{3.8}$$

Therefore, in view of (3.5) and (3.8), the residual can be rewritten as

$$\mathbf{A}(\gamma)\mathbf{U}_{pw} - \mathbf{F}_{pw} = \tilde{\mathbf{J}}(u_{pw})\boldsymbol{\gamma} - \mathbf{b},$$

and the optimization problem (3.4) becomes

$$r(\boldsymbol{d}) = \min_{\gamma \in W_h} \left\|\tilde{\mathbf{J}}(u_{pw})\boldsymbol{\gamma} - \mathbf{b}\right\|_K. \tag{3.9}$$

Note that both u_{pw} and $\mathbf{b}$ depend on the direction $\boldsymbol{d}$.

We can choose the plane waves, with directions

$$\boldsymbol{d}_j = \begin{cases} (\cos\varphi_j, \sin\varphi_j)^{\mathrm{T}} & \text{for } d = 2; \\ (\cos\varphi_{j_1}\sin\theta_{j_2}, \sin\varphi_{j_1}\sin\theta_{j_2}, \cos\theta_{j_2})^{\mathrm{T}} & \text{for } d = 3, \end{cases} \tag{3.10}$$

where the angles $\varphi_j \in [0, 2\pi)$ and $\theta_j \in [0, \pi)$ are generally chosen as a uniform partition of the entire space, that is,

$$\begin{cases} \varphi_j = (j-1)\frac{2\pi}{J}, & j = 1, \cdots, J, \text{ for } d = 2, \\ \varphi_{j_1} = (j_1 - 1)\frac{2\pi}{J_1},\ \theta_{j_2} = (j_2 - 1)\frac{\pi}{J_2}, & j_1 = 1, \cdots, J_1,\ j_2 = 1, \cdots, J_2, \text{ for } d = 3. \end{cases} \tag{3.11}$$

In numerical experiments of Section 5, we will uniformly sample the directions $\boldsymbol{d}_j$ according to (3.11). The numerical results show that such selection is sufficiently effective. We denote the plane wave with direction $\boldsymbol{d}_j$ by $u_j = e^{\mathbf{i}k\boldsymbol{x}\cdot\boldsymbol{d}_j}$ and let $\mathbf{U}_j$ be the vector generated by the degrees of freedom of $I_h u_j$, that is,

$$I_h u_j = I_h(e^{\mathbf{i}k\boldsymbol{x}\cdot\boldsymbol{d}_j}) = \sum_{i=1}^{N} (\mathbf{U}_j)_i \phi_i.$$

Moreover, we denote $\tilde{\mathbf{J}}_j = \tilde{\mathbf{J}}(u_j)$ and $\mathbf{b}_j = \mathbf{b}(\boldsymbol{d}_j) = \mathbf{F}_{pw}(\boldsymbol{d}_j) - \mathbf{A}_0\mathbf{U}_j$. Then the numerical penalty parameter for the CIP-FEM can be obtained by solving the following minimization problem:

$$\gamma_1^{\mathrm{num}} = \arg\min_{\gamma \in W_h} g(\boldsymbol{\gamma}) := \arg\min_{\gamma \in W_h} \sum_{j=1}^{J} \left\|\tilde{\mathbf{J}}_j\boldsymbol{\gamma} - \mathbf{b}_j\right\|_K^2. \tag{3.12}$$

The object function in (3.12) is a quadratic function with respect to $\boldsymbol{\gamma}$, the minimum of g is obtained when the gradient $\nabla_{\boldsymbol{\gamma}} g = 0$, which yields a linear system of $\boldsymbol{\gamma}$:

$$\mathrm{Re} \sum_{j=1}^{J} \tilde{\mathbf{J}}_j^{\mathrm{H}} K\big(\tilde{\mathbf{J}}_j\boldsymbol{\gamma} - \mathbf{b}_j\big) = 0, \tag{3.13}$$

where $\tilde{\mathbf{J}}_j^{\mathrm{H}}$ denotes the Hermitian transpose of $\tilde{\mathbf{J}}_j$.

The procedure for determining the numerical penalty parameter is presented in Algorithm 3.1.

Algorithm 3.1 The numerical penalty parameter defined in (3.12).

Given: The wave number k; the number of directions J or $J = J_1 J_2$; a mesh (satisfying $kh/p \leq 1$).

1: Assemble the stiffness matrix $\mathbf{A}_0$ by (2.4).
2: Determine directions $\boldsymbol{d}_j$ by (3.10)–(3.11) for $j = 1, 2, \cdots, J$, and denote $u_j = e^{\mathbf{i}k\boldsymbol{x}\cdot\boldsymbol{d}_j}$.
3: Compute $\mathbf{b}_j = \mathbf{F}_{pw}(\boldsymbol{d}_j) - \mathbf{A}_0\mathbf{U}_j$ and assemble $\tilde{\mathbf{J}}_j = \tilde{\mathbf{J}}(u_j)$ by (3.7).
4: Solve $\boldsymbol{\gamma}$ from the linear system (3.13) and set $\gamma_1^{\mathrm{num}} = \sum_{i=1}^{M} \boldsymbol{\gamma}_i \psi_i$.

Output: γ_1^{num}.

Remark 3.1. Some explanations for Algorithm 3.1 are as follows.

(1) The mesh condition $kh/p \leq 1$ says that at least 2π degrees of freedom are set per wave length. This is necessary to ensure the accuracy of linear finite element.

(2) The algorithm does not rely on structured mesh, the numerical experiments in Section 5 show that Algorithm 3.1 is effective for not only the structured meshes but also the unstructured meshes. However, the numerical penalty parameter γ_1^{num} is defined on all the interior edges/faces of the mesh, which means that if the mesh changes, the penalty parameter should be recalculated.

(3) According to (3.4), γ_1^{num} actually minimizes the residual $\mathbf{A}(\gamma)\mathbf{U}_{pw} - \mathbf{F}$, so for structured meshes, the numerical parameter γ_1^{num} is no less effective than the theoretical parameter which is obtained by dispersion analysis.

(4) The number of unkowns in (3.13) is related to the number of interior edges/faces and the order of elements, which brings large computational cost when h is small and p is large. Fortunately, this offline phase only needs to be computed once for a given mesh. The resulting interior penalty parameter can be stored and reused for various source functions and different wave numbers no larger than k in online steps. This practice indeed enhances the performance when a substantial number of online computations are required.

(5) For scenarios involving piecewise or variable medium $k(x)$, such as two-layer medium problems, the proposed algorithms in this paper remain viable once the penalty parameters are computed using the maximum wave number $k = \max_{x\in\Omega} k(x)$ during the offline stage.

(6) It is possible to choose the penalty parameters with negative imaginary parts so that the CIP-FEM is absolutely stable [18, 20].

4. Error-minimization approach based on optimization

In this section, we introduce an error-minimization approach with a quasi-Newton iteration algorithmin offline phase to enhance the performance of the optimized CIP-FEM for both linear and higher-order finite elements in online steps. The numerical tests indicate that applying the residual-minimization approach, as discussed in Section 3, to higher-order CIP-FEMs does not lead to a further reduction in pollution errors compared to the linear CIP-FEM. The proposed error-minimization approach and quasi-Newton iteration algorithm address this limitation, aiming to improve the performance of both linear and higher-order CIP-FEMs and effectively reduce pollution errors.

4.1. The error-minimization approach

In the previous section, we define numerical penalty parameter by (3.12) through minimizing the residual of CIP finite element equation. Algorithm 3.1 works well for $p = 1$, however, the algorithm may not work well for $p > 1$. Indeed, although we minimize the residual

$$\mathbf{A}(\gamma)\mathbf{U}_{pw} - \mathbf{F}_{pw},$$

the difference between the plane wave $\mathbf{U}_{pw}$ and the CIP finite element solution $\mathbf{A}^{-1}\mathbf{F}_{pw}$ may still be large. This inspires us to define the objective function by

$$g_j(\gamma) := \left\|\mathbf{U}_j - \mathbf{A}(\gamma)^{-1}\mathbf{F}_j\right\|_K^2, \tag{4.1}$$

where $\mathbf{F}_j = \mathbf{F}_{pw}(\boldsymbol{d}_j)$. Then, we can define the numerical penalty parameter for CIP-FEM by minimizing $g_j(\gamma)$, namely,

$$\gamma_2^{\text{num}} := \arg\min_{\gamma\in W_h} g(\gamma) = \arg\min_{\gamma\in W_h} \sum_{j=1}^{J} g_j(\gamma). \tag{4.2}$$

Note that $g_j(\gamma)$ is no more a quadratic function with respect to γ. In order to minimize such a nonlinear function, some iterative methods are considered. In the next subsection, we will introduce the quasi-Newton method to solve (4.2). To do this, we first give the gradient of $g_j(\gamma)$ in the following lemma.

Lemma 4.1. *There holds*

$$\nabla_\gamma g_j(\gamma) = 2\,\mathrm{Re}\ \tilde{\mathbf{J}}(w_j)^{\mathrm{H}}\mathbf{A}(\gamma)^{-\mathrm{H}}K\mathbf{r}_j, \tag{4.3}$$

where $w_j = \sum_{i=1}^{N}(\mathbf{w}_j)_i\phi_i$ *with* $\mathbf{w}_j = \mathbf{A}(\gamma)^{-1}\mathbf{F}_j$, *and* $\mathbf{r}_j = \mathbf{U}_j - \mathbf{w}_j$.

Proof. By taking the derivative with respect to i-th component, we can obtain

$$\begin{aligned}\frac{\partial g_j}{\partial n_i}(\gamma) &= \lim_{\varepsilon\to 0}\frac{g(\gamma+\varepsilon n_i)-g(\gamma)}{\varepsilon}\\ &= \mathbf{F}_j^{\mathrm{H}}\Big(\mathbf{A}^{-\mathrm{H}}K\frac{\partial\mathbf{A}^{-1}}{\partial n_i} + \Big(\frac{\partial\mathbf{A}^{-1}}{\partial n_i}\Big)^{\mathrm{H}}K\mathbf{A}^{-1}\Big)\mathbf{F}_j - \Big(\mathbf{F}_j^{\mathrm{H}}\Big(\frac{\partial\mathbf{A}^{-1}}{\partial n_i}\Big)^{\mathrm{H}}K\mathbf{U}_j + \mathbf{U}_j^{\mathrm{H}}K\frac{\partial\mathbf{A}^{-1}}{\partial n_i}\mathbf{F}_j\Big)\\ &= 2\,\mathrm{Re}\,(\mathbf{A}^{-1}\mathbf{F}_j - \mathbf{U}_j)^{\mathrm{H}}K\frac{\partial\mathbf{A}^{-1}}{\partial n_i}\mathbf{F}_j.\end{aligned}$$

Noting that

$$\frac{\partial\mathbf{A}^{-1}}{\partial n_i} = -\mathbf{A}^{-1}\frac{\partial\mathbf{A}}{\partial n_i}\mathbf{A}^{-1},$$

and $\mathbf{A}(\gamma)\mathbf{v} = (\mathbf{A}_0 + \mathbf{J}(\gamma))\mathbf{v} = \mathbf{A}_0\mathbf{v} + \tilde{\mathbf{J}}(v)\boldsymbol{\gamma}$ by (3.8), we have

$$\frac{\partial\mathbf{A}}{\partial n_i}(\gamma)\mathbf{v} = \tilde{\mathbf{J}}(v)n_i \quad \text{for any } v = \sum_{i=1}^{N}\mathbf{v}_i\phi_i.$$

Therefore, we arrive at

$$\frac{\partial\mathbf{A}^{-1}}{\partial n_i}\mathbf{F}_j = -\mathbf{A}^{-1}\frac{\partial\mathbf{A}}{\partial n_i}(\gamma)\mathbf{w}_j = -\mathbf{A}^{-1}\tilde{\mathbf{J}}(w_j)n_i,$$

and

$$\frac{\partial g_j}{\partial n_i}(\gamma) = 2\,\mathrm{Re}\ \mathbf{r}_j^{\mathrm{H}}K\mathbf{A}(\gamma)^{-1}\tilde{\mathbf{J}}(w_j)n_i.$$

This completes the proof of this lemma. □

4.2. The quasi-Newton algorithm

The quasi-Newton method [55, §6] is one of the most effective iterative method for solving nonlinear problems. It requires only the gradient of the objective function to be supplied at each iteration. The iteration can be represented as

$$\gamma_{n+1} = \gamma_n + \alpha_n p_n \quad \text{for } n \geq 0, \tag{4.4}$$

where α_n and p_n are step length and search direction, respectively. In general, the search direction has the form

$$p_n = -H_n\nabla_\gamma g(\gamma_n),$$

where H_n is an approximation of the inverse of Hessian matrix $\nabla^2_\gamma g(\gamma_n)$. The matrix H_n is obtained by the BFGS method [56], which is one of the most popular quasi-Newton algorithm. Moreover, since H_n is dense and large, it is too expensive to identify this matrix. We adopt the limited-memory BFGS (L-BFGS) method (see, e.g., [57] and [55, §7.2]) to reduce the storage and calculation. In addition,

the step length α_n can be obtained by inexact line search [55, §3] for the global minimizer of the objective function $g(\gamma)$:

$$\alpha_n = \arg\min_{\alpha\in\mathbb{R}} g(\gamma_n + \alpha p_n). \tag{4.5}$$

The quasi-Newton algorithm to determine the numerical penalty parameter for the optimized CIP-FEM is presented in Algorithm 4.1.

Algorithm 4.1 The numerical penalty parameter defined in (4.2).

Given: The wave number k; the directions $\boldsymbol{d}_j$ as (3.10)–(3.11); a mesh (satisfying $kh/p \le 1$); the tolerances ϵ_1 and ϵ_2 and the maximum number of iterations $m_{\rm it}$; the initial value γ_0; set $n \leftarrow 0$.

1: **repeat**
2: Compute $\nabla g_n = \nabla_\gamma g(\gamma_n)$ by (4.3) and denote $g_n = g(\gamma_n)$.
3: Compute the search direction $p_n = -H_n \nabla g_n$ by L-BFGS method.
4: Compute step length α_n by line search (4.5).
5: $\gamma_{n+1} \leftarrow \gamma_n + \alpha_n p_n$.
6: If $\|\nabla g_n\| < \varepsilon_1$ or $|g_n - g_{n-1}| < \varepsilon_2$ $(n \ge 1)$, stop; otherwise, $n \leftarrow n+1$.
7: **until** $n = m_{\rm it}$.

Output: $\gamma_2^{\rm num} = \gamma_n$.

Remark 4.2. The choice of the initial value γ_0 is flexible. One reasonable choice is to use the numerical parameter $\gamma_1^{\rm num}$ given by Algorithm 3.1. Another simpler choice is let $\gamma_0 \equiv (C_1, C_2, \cdots, C_p)^{\rm T}$ be a constant vector for all $e \in \mathcal{E}_h^{\rm I}$. Such a choice is often used for meshes that are approximately structured.

5. Numerical experiments

In this section, we present numerical tests to illustrate the performance of the proposed algorithms in reducing pollution errors on both structured and unstructured meshes. To showcase the practical applicability of our approach, we specifically examine the simulation of high-frequency acoustic fields within a vehicle cabin, characterized by its complex geometry that cannot be partitioned into structured meshes. The numerical results obtained from this car cabin example highlight the potential and effectiveness of our proposed methods in accurately modeling and predicting acoustic behavior in real-world scenarios. In the following numerical tests, we use the L^2-norm and H^1-norm to determine the numerical parameters $\gamma^{\rm num}$ given by Algorithm 3.1 and Algorithm 4.1, respectively.

5.1. Performance evaluation of Algorithm 3.1

In this subsection, we consider the linear CIP-FEM with the numerical penalty parameters $\gamma^{\rm num} = \gamma_1^{\rm num}$ given by Algorithm 3.1 and compare it with the linear FEM and the linear CIP-FEM with the theoretical parameters as

$$\gamma^{\#} = \begin{cases} -\frac{\sqrt{3}}{24} - \frac{\sqrt{3}}{1728}(kh)^2 & \text{for equilateral triangulation;} \\ -0.08592096810583184 & \text{for Cartesian mesh,} \end{cases} \tag{5.1}$$

which are derived in [52] and [21], respectively. The directions $\boldsymbol{d}_j$ in Algorithm 3.1 are chosen according to (3.10)–(3.11) with $J = 12$ for $d = 2$ and $J_1 = 12, J_2 = 6$ for $d = 3$.

Example 5.1. In this example, we consider the exact solution given by:

$$u = \cos(k|x|) \ \text{ for } x \in \Omega, \tag{5.2}$$

and let $f = -\Delta u - k^2 u$ in Ω and $g = \partial_{\mathbf{n}} u - \mathbf{i}ku$ on $\partial\Omega$ represent the corresponding source and impedance boundary values, respectively. We investigate two types of meshes: triangular meshes and quadrilateral meshes, including both structured and unstructured configurations. These meshes are represented as (a)-(d) in Figure 5.1.

Setting $k_{\max} = 500$, we refine the four sample meshes in Figure 5.1 to have sizes $\hbar \approx 1/k_{\max}$, where $\hbar$ denotes the maximum length of all edges in the mesh. By utilizing Algorithm 3.1 with $k = k_{\max}$, we calculate and save the four numerical penalty parameters γ^{num} for the refined meshes.

Figure 5.1 displays the relative H^1-errors of the finite element interpolation, the FEM ($\gamma = 0$), the CIP-FEM with the theoretical parameter $\gamma = \gamma^{\#}$, and the CIP-FEM with the numerical parameter $\gamma = \gamma^{\text{num}}$, plotted against the increasing wave number k up to $k_{\max}$. From Figure 5.1, the following observations can be made:

(i) As the wave number increases, the errors of the standard FEM grow super-linearly. After the wave number reaches a certain threshold, typically less than 100, the error plots of the FEM no longer align with those of the corresponding finite element interpolation. This behavior clearly demonstrates the impact of pollution errors associated with the standard FEM. In contrast, both the theoretical and numerical CIP-FEM parameters can significantly reduce pollution errors.

(ii) For the structured meshes (a) and (c), the CIP-FEM with the numerical parameter γ^{num} performs as well as the one with the theoretical parameter $\gamma^{\#}$, and the pollution errors remain negligible for k up to $k_{\max}$. Moreover, the mean values of the numerical parameters γ^{num} are approximately -0.0729388 for equilateral triangulation and -0.0852447 for the Cartesian mesh, which are close to the theoretically optimal parameters in (5.1).

(iii) For the unstructured meshes (b) and (d), the CIP-FEM with the numerical parameter γ^{num} outperforms the one with the theoretical parameter $\gamma^{\#}$ for sufficiently large k. The pollution errors of the CIP-FEM with $\gamma = \gamma^{\text{num}}$ are nearly imperceptible for k up to $k_{\max}$, while the pollution errors of the CIP-FEM with $\gamma = \gamma^{\#}$ become noticeable when k exceeds a value greater than 200.

Example 5.2. In this example, we consider the Helmholtz scattering problem involving a bounded, sound soft obstacle occupying a nonconvex domain $D \subset \mathbb{R}^2$:

$$\begin{aligned} \Delta u + k^2 u = 0 \quad &\text{in } \mathbb{R}^2 \setminus \overline{D}, \\ u = 0 \quad &\text{on } \partial D \end{aligned}$$

with the Sommerfeld radiation condition

$$\frac{\partial (u - u^{\text{inc}})}{\partial r} - \mathbf{i}k(u - u^{\text{inc}}) = o(r^{-1/2}) \quad \text{as } r = |x| \to \infty,$$

which will be approximated using the perfectly matched layer (PML) technique (see, e.g., [5]). Let the incident wave be $u^{\text{inc}} = 20\exp(-\mathbf{i}kx_1)$, which is a plane wave originating from the east of the scatterer. The wave number is $k = 500$ and the mesh size is about $\hbar = 1/500$. In Figure 5.2 we plot the magnitude of the finite element solution and the CIP-finite element solutions for the total field u. The reference solution is obtained by solving the equation with higher-order FEM ($p = 3$). The figure clearly illustrates that the CIP-finite element solution with the numerical parameter provides a much closer approximation to the reference solution compared to the other methods employed.

Example 5.3. In this example, we examine a three-dimensional problem with an exact solution identical to that of Example 5.1. The structured and unstructured tetrahedral meshes used in this example are displayed on the left side of Figure 5.3. Currently, the theoretical optimal parameter for this case remains unknown. The meshes labeled (a) and (b) in Figure 5.3 are refined to sizes of approximately $\hbar = 0.0216506$ and $\hbar = 0.0340198$, respectively.

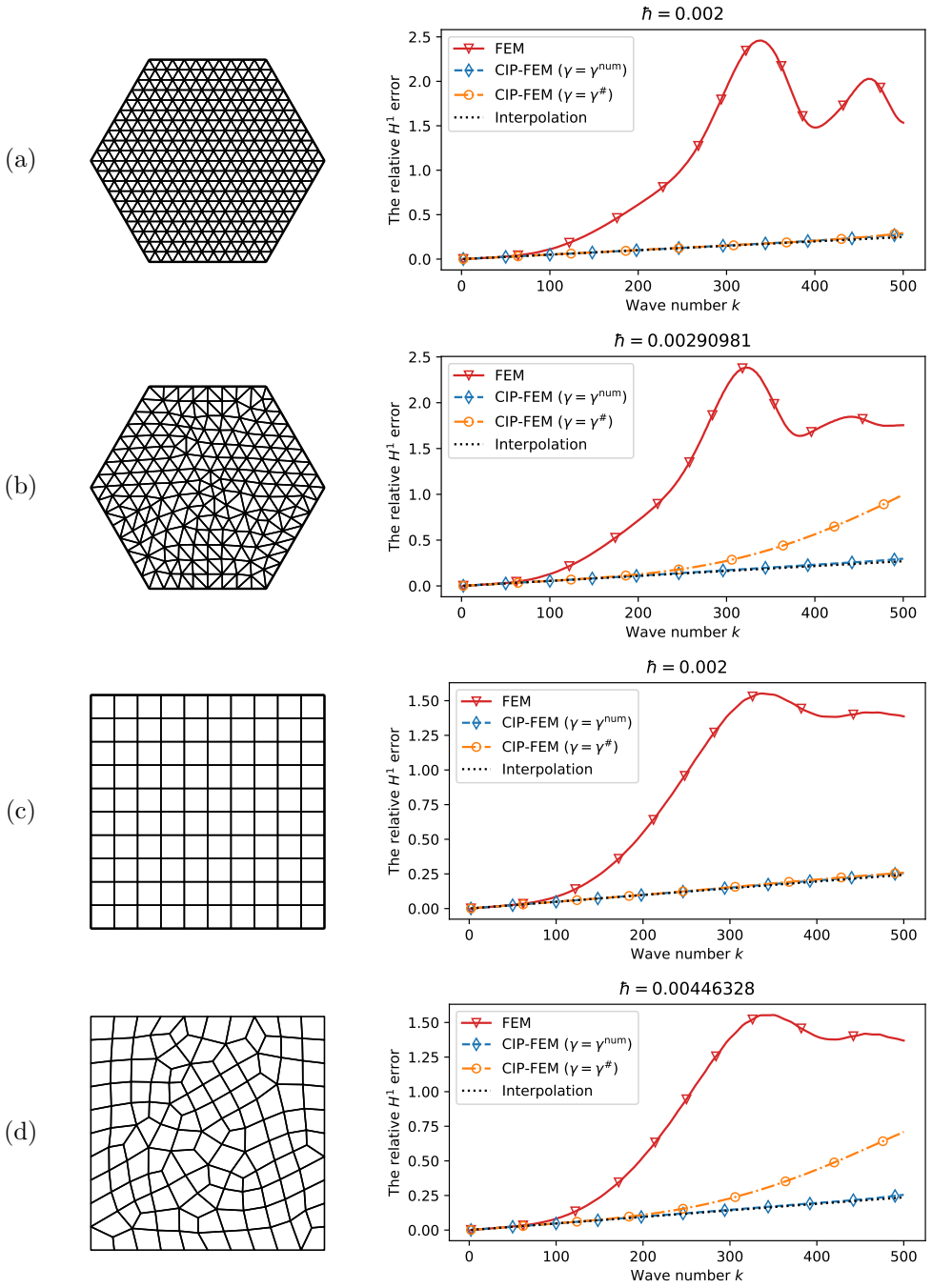

Fig. 5.1: Comparisons of the relative H^1-errors of the finite element interpolation, the FEM ($\gamma = 0$), and the CIP-FEMs with theoretical and numerical penalty parameters on the triangular meshes and quadrilateral meshes.

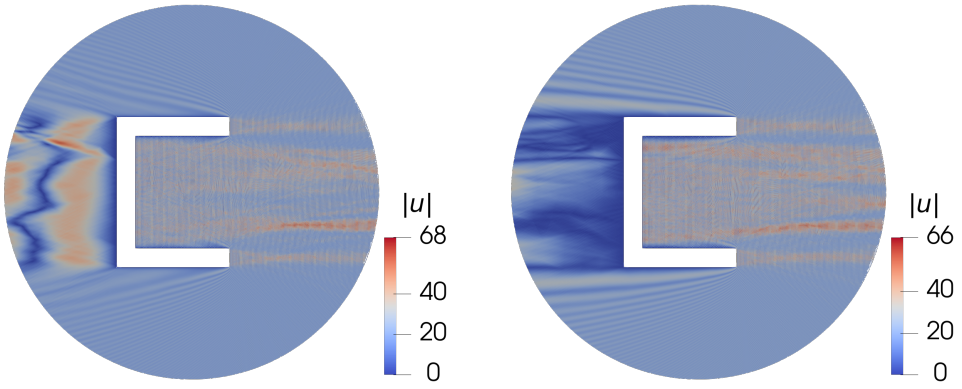

(A) FEM (B) CIP-FEM ($\gamma = \gamma^{\#}$)

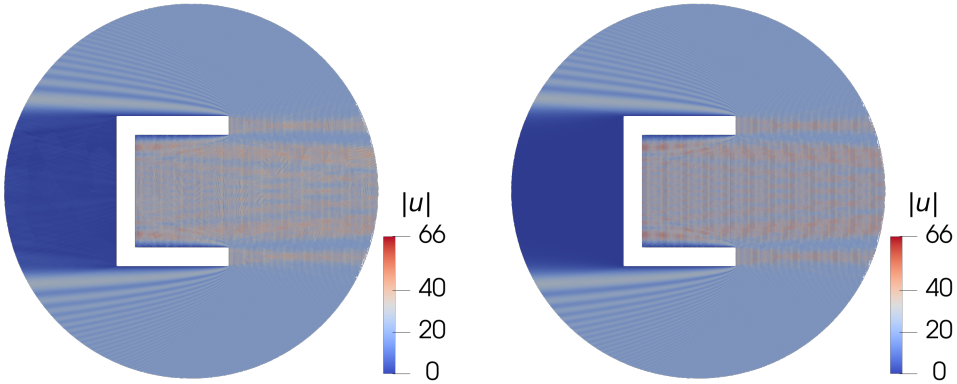

(C) CIP-FEM ($\gamma = \gamma^{\mathrm{num}}$) (D) Reference solution

Fig. 5.2: The total field of the scattering problem.

For these refined meshes, we determine two numerical parameters $\gamma = \gamma^{\mathrm{num}}$ using Algorithm 3.1 with $k = 60$. The right side of Figure 5.3 presents the relative H^1-errors of the finite element interpolation, the FEM, and the CIP-FEM with the numerical parameters. It is evident that the pollution errors are significantly diminished by employing the CIP-FEM with the numerical penalty parameter.

All the numerical results in this subsection demonstrate the effectiveness of the proposed algorithm, namely, Algorithm 3.1, for both structured and unstructured meshes. By employing the linear CIP-FEM with the numerical penalty parameters obtained from Algorithm 3.1, the pollution errors can be significantly reduced. In addition, it can be observed that penalty parameters computed with wave number $k = k_{\max}$ prove effective for all $k \leq k_{\max}$. This is an evidence of the statements in Remark 3.1 (4) and (5).

5.2. Performance evaluation of Algorithm 4.1

Next, we consider the higher-order CIP-FEM with the numerical penalty parameters given by Algorithm 4.1.

Example 5.4. In this example, we investigate the performance of high-order CIP-FEMs on equilateral triangulations (Figure 5.1(a)), refined to satisfy $k_{\max}\hbar/p = 1$ for $p = 2, 3$. We set $k_{\max} = 600$ and consider the exact solution defined as (5.2). The numerical parameters $\gamma_0 = \gamma_1^{\mathrm{num}}$ and $\gamma^{\mathrm{num}} = \gamma_2^{\mathrm{num}}$

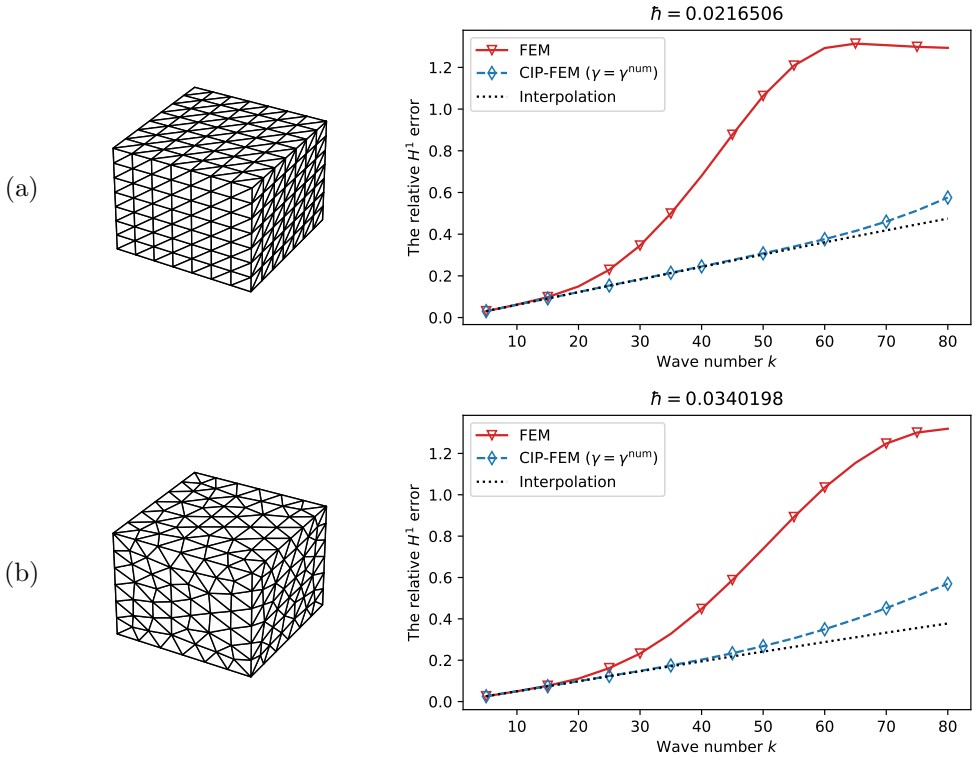

Fig. 5.3: Comparisons of the relative H^1-errors of the interpolation, the FEM ($\gamma = 0$), and the CIP-FEM ($\gamma = \gamma^{\mathrm{num}}$). Upper: structured mesh. Lower: unstructured mesh.

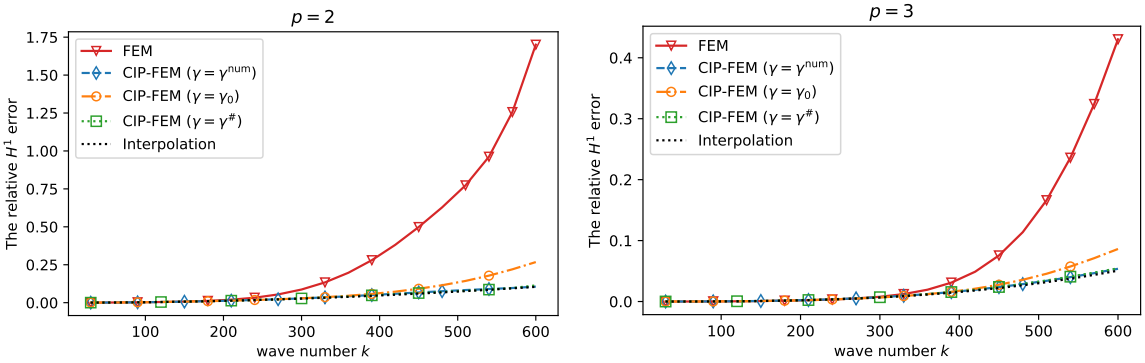

Fig. 5.4: Comparisons of the relative H^1-errors of FEM and CIP-FEMs with numerical penalty parameters γ^{num} and γ_0, and with theoretical penalty parameters $\gamma^{\#}$ on the equilateral triangulations satisfying $k_{\max}\hbar/p = 1$. Left: $p = 2$. Right: $p = 3$.

are obtained using Algorithm 3.1 and Algorithm 4.1 (with initial value γ_0), respectively. Figure 5.4 depicts the relative H^1-errors for the FEM ($\gamma = 0$), the CIP-FEM with penalty parameter $\gamma = \gamma_0$, and the CIP-FEM with penalty parameter $\gamma = \gamma^{\mathrm{num}}$. The results demonstrate that the CIP-FEM with numerical parameters γ^{num} outperforms the standard FEM and the CIP-FEM with initial numerical parameters γ_0, and is comparable to the CIP-FEM with theoretical parameters $\gamma^{\#}$ (derived in [53] for $p = 2, 3$).

Example 5.5. In this example, we focus on the second-order CIP-FEM ($p = 2$) with both theoretical

and numerical penalty parameters on an unstructured mesh, as shown in the left of Figure 5.5. For this case, we utilize the theoretical penalty parameter derived for the equilateral triangulation in [53]. The numerical penalty parameter is obtained using Algorithm 4.1. The exact solution is defined as (5.2), and the mesh is refined to have a maximum length $\hbar \approx 5.87 \times 10^{-3}$. The relative H^1-errors presented in the right of Figure 5.5 clearly demonstrate that the CIP-FEM with the numerical penalty parameter is more effective in reducing errors compared to both the FEM and the CIP-FEM with the theoretical penalty parameter.

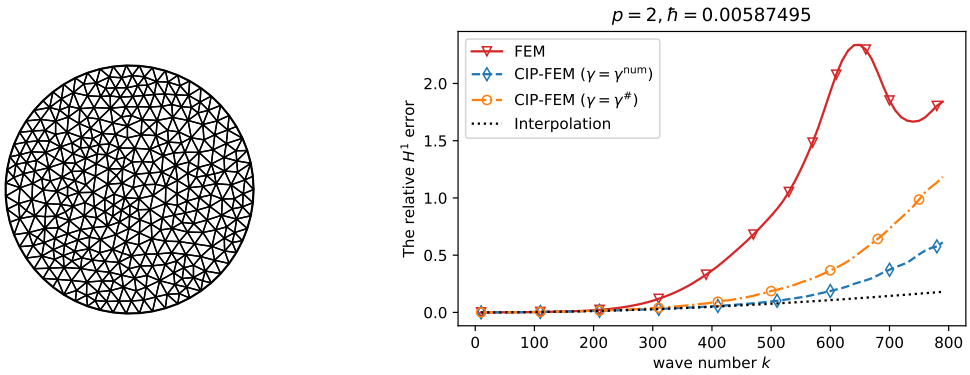

Fig. 5.5: Comparisons of the relative H^1-errors of the interpolation, the FEM, and the CIP-FEMs with theoretical and numerical penalty parameters on a unstructured mesh.

5.3. Numerical simulation of high-frequency acoustic fields in a vehicle cabin

In this subsection, we conduct a numerical simulation of high-frequency acoustic fields inside a vehicle cabin using a model [1] adapted from the COMSOL software [58]. The geometry of the cabin and the corresponding mesh used in the simulation are shown in Figure 5.6.

Two different meshes are considered: the first one, denoted as `mesh1`, consists of 226,570 cells and 44,614 vertices, with a mesh size of approximately $\hbar \approx 0.101$ (see Figure 5.6(B)). The second mesh, referred to as `mesh2`, comprises 1,465,699 cells and 261,886 vertices, with a mesh size of approximately $\hbar \approx 0.058$. The numerical penalty parameters utilized in this simulation are determined using Algorithm 4.1.

Example 5.6. In this example, we solve the Helmholtz equation given by

$$\begin{cases} -\dfrac{1}{\rho}\Delta u - \dfrac{k^2}{\rho}u = f & \text{in } \Omega, \\ \dfrac{1}{\rho}\dfrac{\partial u}{\partial \mathbf{n}} + \dfrac{i\omega}{Z}u = g & \text{on } \partial\Omega, \end{cases} \tag{5.3}$$

where $k = \omega/c = 2\pi\nu/c$ represents the wave number, ν is the frequency, c is the speed of sound, ρ is the air density, and Z is the acoustic impedance.

For this example, we consider a manufactured solution in the form of $u = \sin(k|x|)$. The values of f and g are calculated by substituting the manufactured solution u into equation (5.3). We set $c = 343$, $\rho = 1.2$, and $Z = c$ for this particular test case. In this example, we use linear elements ($p = 1$) on `mesh2` and quadratic elements ($p = 2$) on `mesh1`, so that the ratios $k\hbar/p$ are similar in both cases.

[1] Model file: www.comsol.com/model/car-cabin-acoustics-8212-frequency-domain-analysis-15013

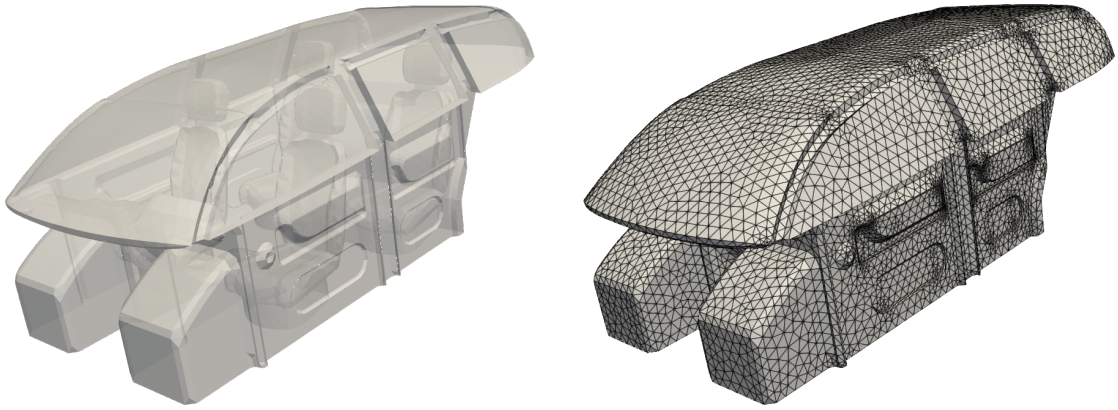

(A) Geomerty (B) Mesh

Fig. 5.6: The geometry and mesh of the cabin.

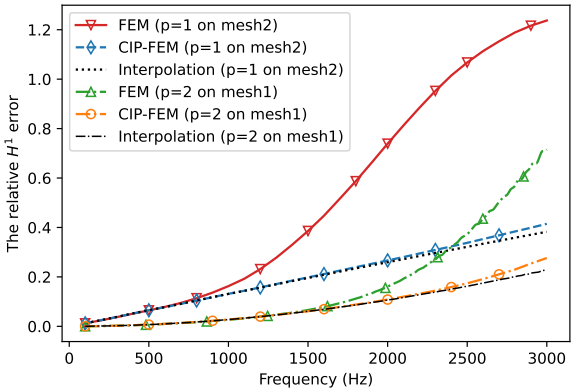

Fig. 5.7: H^1-errors for Example 5.6 with exact solution.

Following the previous experiments, we present the H^1-errors of the FEM, the CIP-FEM, and the finite element interpolation in Figure 5.7. When considering frequencies around 3 kHz for $p = 1$ on `mesh2` and $p = 2$ on `mesh1`, the errors obtained by the CIP-FEM are comparable to the interpolation error. However, the relative errors of the linear FEM and quadratic FEM exceed 100% and 60%, respectively, significantly surpassing the interpolation errors.

To test the efficiency of the proposed method, we plot the errors against computational time for both FEM and CIP-FEM using different meshes. The results for $k = 40$ and $k = 60$ are shown in Figure 5.8, and the data points are labeled with the corresponding number of degrees of freedom (dofs), where $1\text{M} = 1 \times 10^6$. The proposed CIP-FEM demonstrates a reduced computational time to achieve the same level of error compared to FEM.

From the numerical results we see that the proposed CIP-FEM is more effective than the FEM for the three-dimensional simulation in a real vehicle cabin with unstructured meshes, while other CIP-FEMs in the literature typically require structured meshes and therefore cannot be used in this scenario.

Example 5.7. Next, we proceed with the simulation of the sound field inside the car cabin on `mesh1` using the boundary conditions defined in the COMSOL model. In this simulation, we position the sound source at the left midwoofer location.

Figure 5.9 illustrates the sound pressure level (SPL) at a point with coordinates $[2.5, -0.5, 1.2]$

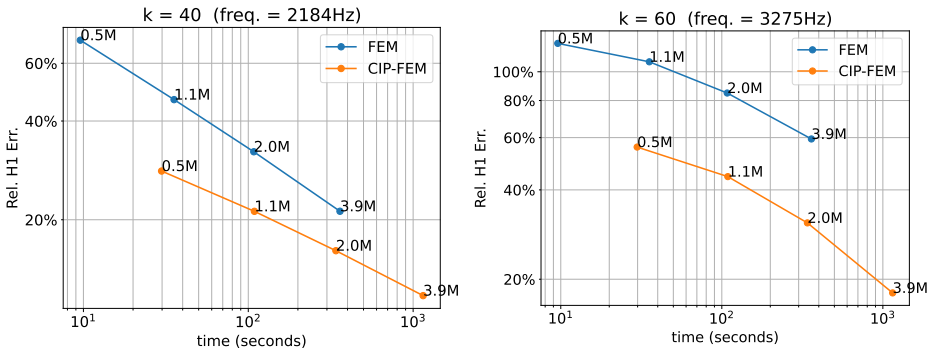

(A) $k = 40$ (B) $k = 60$

Fig. 5.8: The relative errors against the computational time for FEM and CIP-FEM. The points are labeled with the corresponding number of degrees of freedom, where $1\text{M} = 1 \times 10^6$.

(near the driver's head) for different methods and increasing frequencies. The finite element solution with $p = 3$ serves as the reference solution, depicted by the black dotted lines in Figure 5.9. Notably, even at frequencies around 1500 Hz, the SPL values obtained by CIP-FEM with $p = 1$ remain close to those of the reference solution. In contrast, the solution of linear FEM can only accurately approximate the reference solution with respect to the SPL values up to frequencies of 700 Hz. Moreover, for $p = 2$, the solution of CIP-FEM exhibits closer proximity to the reference solution compared to that of FEM. Importantly, the CIP-FEM precisely captures the peaks and troughs of the SPL with greater accuracy.

In the last simulation, we placed a sound source at the right tweeter in the front-right of the car on `mesh1`. Figure 5.10 shows the real part of the solutions obtained using quadratic FEM and CIP-FEM at a frequency of 2.5 kHz on the slice depicted in Figure 5.10(A). To provide a more informative comparison, we overlaid contour lines of the reference solution (Figure 5.10(D)) onto Figures 5.10(B) and (C). As shown in Figure 5.10, the solution obtained by CIP-FEM accurately captures the peaks and troughs of the true solution, while the solution of FEM exhibits a noticeable phase shift. Furthermore, we plotted the real part of the solutions along a line within the slice, which is indicated by the black line in Figure 5.10(A). In Figure 5.11, we denote the distance between the current point and the start point of the line by s. It can be observed that the phase difference between the solution of CIP-FEM and the reference solution is much smaller compared to the phase difference between the solution of FEM and the reference solution. This observation further confirms the effectiveness of the proposed optimized CIP-FEM in accurately simulating high-frequency acoustic fields.

6. Conclusion

We have presented an optimized CIP-FEM approach for effectively reducing pollution errors when solving the Helmholtz equation with high wave numbers. Our method involves determining the interior penalty parameters by minimizing the residual of the CIP finite element equations for plane waves in the offline phase. To further enhance the performance of these penalty parameters, we have introduced an error-minimization approach with a quasi-Newton algorithm for their correction. In practical computations, the resulting interior penalty parameters can be stored and reused for different source functions in online steps. Numerical experiments demonstrate the significant reduction in pollution errors for the proposed algorithms, benefiting both linear and higher-order CIP-FEMs implemented on both structured and unstructured meshes. Notably, our algorithms prove particularly valuable for finite element discretization on general unstructured meshes, where it is not possible to derive the theoretically interior penalty parameters for pollution error reduction through dispersion analysis.

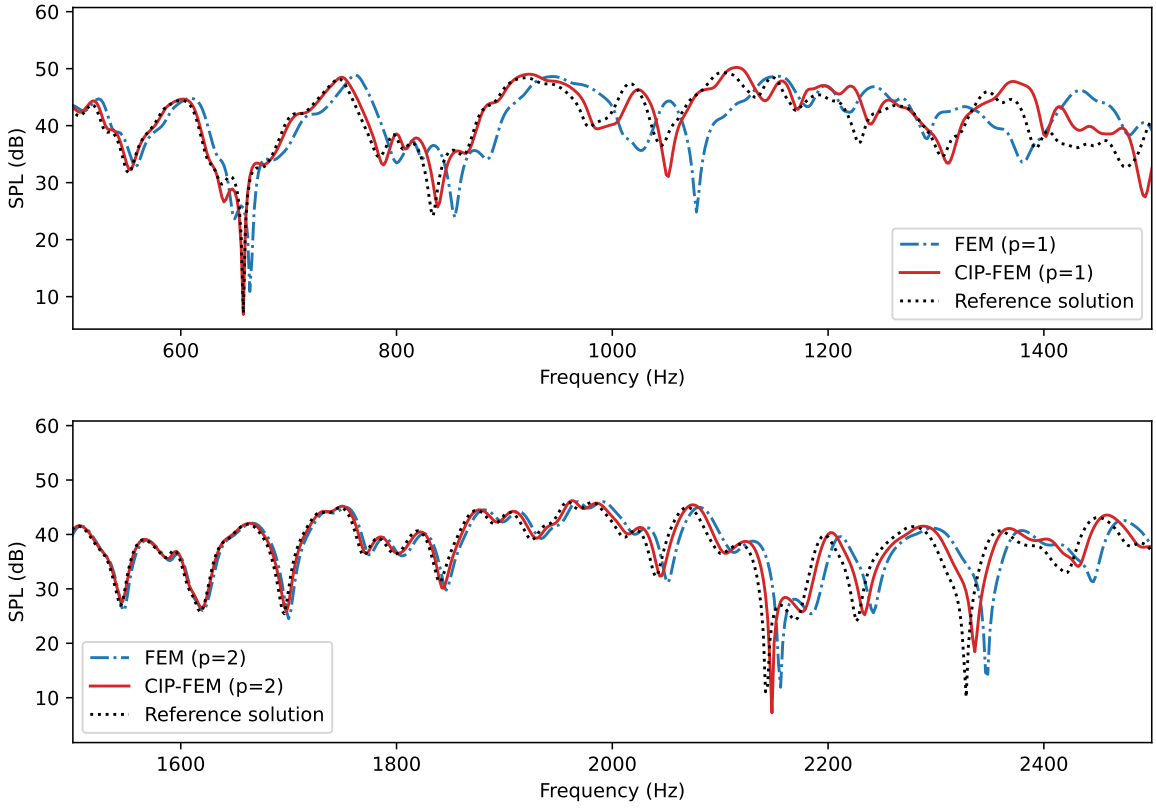

Fig. 5.9: Sound pressure level (SPL) at a point with coordinates $[2.5, -0.5, 1.2]$.

Overall, our optimized CIP-FEM approach offers a robust and efficient solution for accurately solving the Helmholtz equation with high wave numbers on general unstructured meshes, providing reliable results across various mesh configurations for real-world applications with complex geometry.

Acknowledgement

The authors would like to thank Dr. Jiashun Hu for the helpful discussions on the computer implementation of the algorithms. The research is supported in part by a Collaborative Research Project between The Hong Kong Polytechnic University and Huawei Technologies Co., Ltd.

References

[1] S. N. Chandler-Wilde, P. Monk, Wave-number-explicit bounds in time-harmonic scattering, SIAM J. Math. Anal. 39 (5) (2008) 1428–1455.

[2] J. M. Melenk, S. A. Sauter, Convergence analysis for finite element discretizations of the Helmholtz equation with Dirichlet-to-Neumann boundary conditions, Math. Comp. 79 (272) (2010) 1871–1914.

[3] Z. Chen, X. Liu, An adaptive perfectly matched layer technique for time-harmonic scattering problems, SIAM J. Numer. Anal. 43 (2) (2005) 645–671.

[4] J. H. Bramble, J. E. Pasciak, Analysis of a finite element PML approximation for the three dimensional time-harmonic Maxwell problem, Math. Comp. 77 (261) (2008) 1–10.

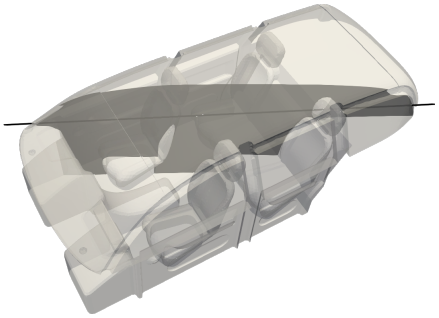

(A) Slice and line

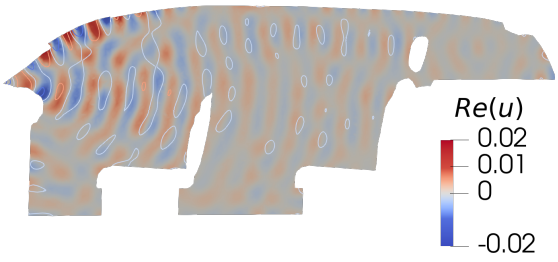

(B) FEM ($p = 2$ on `mesh1`)

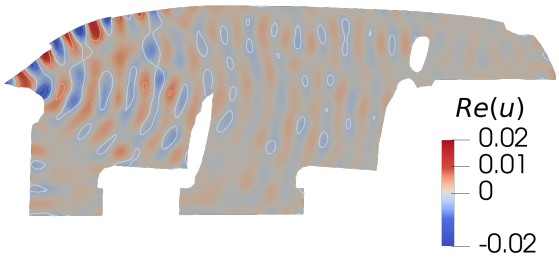

(C) CIP-FEM ($p = 2$ on `mesh1`)

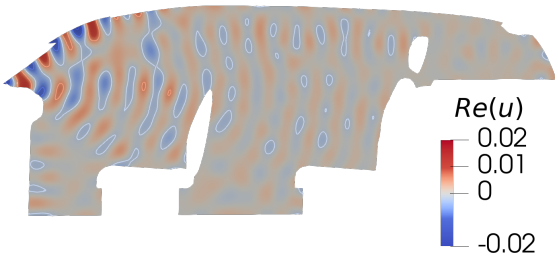

(D) Reference solution

Fig. 5.10: The real part of the solutions on a domain slice at a frequency of 2.5 kHz, comparing the quadratic FEM with CIP-FEM.

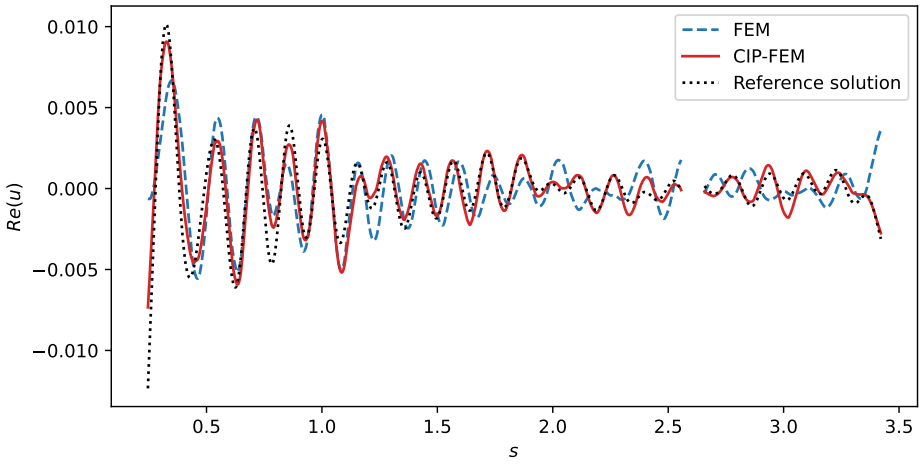

Fig. 5.11: The real part of the solutions along a line shown in Figure 5.10(A). The parameter s represents the distance from the current point to the start point of the line.

[5] Y. Li, H. Wu, FEM and CIP-FEM for Helmholtz equation with high wave number and perfectly matched layer truncation, SIAM J. Numer. Anal. 57 (1) (2019) 96–126.

[6] F. Ihlenburg, Finite Element Analysis of Acoustic Scattering, Vol. 132 of Appl. Math. Sci., Springer-Verlag, New York, 1998.

[7] I. M. Babuška, S. A. Sauter, Is the pollution effect of the FEM avoidable for the Helmholtz equation considering high wave numbers?, SIAM Rev. 42 (3) (2000) 451–484.

[8] A. Deraemaeker, I. Babuška, P. Bouillard, Dispersion and pollution of the FEM solution for the Helmholtz equation in one, two and three dimensions, Int. J. Numer. Meth. Engng. 46 (4) (1999) 471–499.

[9] F. Ihlenburg, I. Babuška, Finite element solution of the Helmholtz equation with high wave number. I. The h-version of the FEM, Comput. Math. Appl. 30 (9) (1995) 9–37.

[10] F. Ihlenburg, I. Babuška, Finite element solution of the Helmholtz equation with high wave number part II: The hp version of the FEM, SIAM J. Numer. Anal. 34 (1) (1997) 315–358.

[11] J. M. Melenk, S. A. Sauter, Wavenumber explicit convergence analysis for Galerkin discretizations of the Helmholtz equation, SIAM J. Numer. Anal. 49 (3) (2011) 1210–1243.

[12] K. Wang, Y. S. Wong, Is pollution effect of finite difference schemes avoidable for multi-dimensional Helmholtz equations with high wave numbers?, Commun. Comput. Phys. 21 (2017) 490–514.

[13] M. Ainsworth, Discrete dispersion relation for hp-version finite element approximation at high wave number, SIAM J. Numer. Anal. 42 (2) (2004) 553–575.

[14] T. Chaumont-Frelet, S. Nicaise, Wavenumber explicit convergence analysis for finite element discretizations of general wave propagation problems, IMA J. Numer. Anal. 40 (2) (2020) 1503–1543.

[15] E. Burman, L. Zhu, H. Wu, Linear continuous interior penalty finite element method for Helmholtz equation with high wave number: One-dimensional analysis, Numer. Meth. Par. Diff. Equ. 32 (5) (2016) 1378–1410.

[16] Y. Du, H. Wu, Preasymptotic error analysis of higher order FEM and CIP-FEM for Helmholtz equation with high wave number, SIAM J. Numer. Anal. 53 (2) (2015) 782–804.

[17] Y. Li, W. Zheng, X. Zhu, A CIP-FEM for high-frequency scattering problem with the truncated DtN boundary condition, CSIAM Trans. Appl. Math. 1 (3) (2020) 530–560.

[18] H. Wu, Pre-asymptotic error analysis of CIP-FEM and FEM for the Helmholtz equation with high wave number. Part I: Linear version, IMA J. Numer. Anal. 34 (3) (2014) 1266–1288.

[19] H. Wu, J. Zou, Finite element method and its analysis for a nonlinear Helmholtz equation with high wave numbers, SIAM J. Numer. Anal. 56 (3) (2018) 1338–1359.

[20] L. Zhu, H. Wu, Preasymptotic error analysis of CIP-FEM and FEM for Helmholtz equation with high wave number. Part II: hp version, SIAM J. Numer. Anal. 51 (3) (2013) 1828–1852.

[21] Y. Zhou, H. Wu, Dispersion Analysis of CIP-FEM for the Helmholtz Equation, SIAM J. Numer. Anal. 61 (3) (2023) 1278–1292.

[22] M. Ainsworth, P. Monk, W. Muniz, Dispersive and dissipative properties of discontinuous Galerkin finite element methods for the second-order wave equation, J. Sci. Comput. 27 (1-3) (2006) 5–40.

[23] H. Chen, P. Lu, X. Xu, A hybridizable discontinuous Galerkin method for the Helmholtz equation with high wave number, SIAM J. Numer. Anal. 51 (4) (2013) 2166–2188.

[24] X. Feng, H. Wu, Discontinuous Galerkin methods for the Helmholtz equation with large wave numbers, SIAM J. Numer. Anal. 47 (4) (2009) 2872–2896.

[25] X. Feng, H. Wu, *hp*-discontinuous Galerkin methods for the Helmholtz equation with large wave number, Math. Comp. 80 (276) (2011) 1997–2024.

[26] X. Feng, Y. Xing, Absolutely stable local discontinuous Galerkin methods for the Helmholtz equation with large wave number, Math. Comp. 82 (283) (2013) 1269–1296.

[27] R. Griesmaier, P. Monk, Error analysis for a hybridizable discontinuous Galerkin method for the Helmholtz equation, J. Sci. Comput. 49 (3) (2011) 291–310.

[28] R. H. Hoppe, N. S. Sharma, Convergence analysis of an adaptive interior penalty discontinuous Galerkin method for the Helmholtz equation, IMA J. Numer. Anal. 33 (1) (2013) 898–921.

[29] J. M. Melenk, A. Parsania, S. A. Sauter, General DG-methods for highly indefinite Helmholtz problems, J. Sci. Comput. 57 (3) (2013) 536–581.

[30] B. Zhu, H. Wu, Preasymptotic error analysis of the HDG method for Helmholtz equation with large wave number, J. Sci. Comput. 87 (2) (2021) 1–34.

[31] L. Mu, J. Wang, X. Ye, A new weak Galerkin finite element method for the Helmholtz equation, IMA J. Numer. Anal. 35 (3) (2014) 1228–1255.

[32] L. Mu, J. Wang, X. Ye, S. Zhao, A numerical study on the weak Galerkin method for the Helmholtz equation, Commun. Comput. Phys. 15 (5) (2014) 1461–1479.

[33] Y. Du, Z. Zhang, A numerical analysis of the weak Galerkin method for the Helmholtz equation with high wave number, Commun. Comput. Phys. 22 (1) (2017) 133–156.

[34] C. J. Gittelson, R. Hiptmair, I. Perugia, Plane wave discontinuous Galerkin methods: Analysis of the *h*-version, ESAIM: M2AN 43 (2) (2009) 297–331.

[35] R. Hiptmair, A. Moiola, I. Perugia, Plane wave discontinuous Galerkin methods for the 2D Helmholtz equation: Analysis of the *p*-version, SIAM J. Numer. Anal. 49 (1) (2011) 264–284.

[36] R. Hiptmair, A. Moiola, I. Perugia, Trefftz discontinuous Galerkin methods for acoustic scattering on locally refined meshes, Appl. Numer. Math. 79 (2014) 79–91.

[37] R. Hiptmair, A. Moiola, I. Perugia, Plane wave discontinuous Galerkin methods: Exponential convergence of the *hp*-version, Found. Comput. Math. 16 (3) (2016) 637–675.

[38] R. Hiptmair, A. Moiola, I. Perugia, A survey of Trefftz methods for the Helmholtz equation, in: Building Bridges: Connections and Challenges in Modern Approaches to Numerical Partial Differential Equations, Springer, 2016, pp. 237–279.

[39] S. Kapita, P. Monk, A plane wave discontinuous Galerkin method with a Dirichlet-to-Neumann boundary condition for the scattering problem in acoustics, J. Comput. Appl. Math. 327 (2018) 208–225.

[40] C. J. Gittelson, R. Hiptmair, Dispersion analysis of plane wave discontinuous Galerkin methods, Int. J. Numer. Meth. Engng. 98 (5) (2014) 313–323.

[41] D. L. Brown, D. Gallistl, D. Peterseim, Multiscale Petrov-Galerkin method for high-frequency heterogeneous Helmholtz equations, in: M. Griebel, M. A. Schweitzer (Eds.), Meshfree Methods for Partial Differential Equations VIII, Lecture Notes in Computational Science and Engineering, Springer International Publishing, 2017, pp. 85–115.

[42] H. Cao, H. Wu, IPCDGM and multiscale IPDPGM for the Helmholtz problem with large wave number, J. Comput. Appl. Math. 369 (2020) 1–19.

[43] D. Gallistl, D. Peterseim, Stable multiscale Petrov–Galerkin finite element method for high frequency acoustic scattering, Comput. Methods Appl. Mech. Engrg. 295 (2015) 1–17.

[44] D. Peterseim, Eliminating the pollution effect in Helmholtz problems by local subscale correction, Math. Comp. 86 (305) (2016) 1005–1036.

[45] K. Wang, Y. S. Wong, Pollution-free finite difference schemes for non-homogeneous Helmholtz equation., Int. J. Numer. Anal. Mod. 11 (4) (2014) 787–815.

[46] K. Wang, Y. S. Wong, J. Deng, Efficient and accurate numerical solutions for Helmholtz equation in polar and spherical coordinates, Commun. Comput. Phys. 17 (3) (2015) 779–807.

[47] B. Han, M. Michelle, Y. S. Wong, Dirac assisted tree method for 1D heterogeneous Helmholtz equations with arbitrary variable wave numbers, Comput. Math. Appl. 97 (2021) 416–438.

[48] L. P. Franca, A. P. Macedo, A two-level finite element method and its application to the Helmholtz equation, Int. J. Numer. Meth. Engng. 43 (1) (1998) 23–32.

[49] L. P. Franca, C. Farhat, A. P. Macedo, M. Lesoinne, Residual-free bubbles for the Helmholtz equation, Int. J. Numer. Meth. Engng. 40 (21) (1997) 4003–4009.

[50] L. L. Thompson, P. M. Pinsky, A Galerkin least-squares finite element method for the two-dimensional Helmholtz equation, Int. J. Numer. Meth. Engng. 38 (3) (1995) 371–397.

[51] J. Douglas, T. Dupont, Interior penalty procedures for elliptic and parabolic Galerkin methods, Lect. Notes Phys. 58 (1976) 207–216.

[52] C. Han, Dispersion analysis of the IPFEM for the Helmholtz equation with high wave number on equilateral triangular meshes, Master's thesis, Nanjing University (2012).

[53] Y. Zhou, Dispersion analysis of CIP-FEM for Helmholtz equation, Ph.D. thesis, Nanjing University (2023).

[54] D. Zhang, Optimal penalty parameters for interior penalty finite element methods for Helmholtz equation on triangular meshes., Master's thesis, Nanjing University (2015).

[55] J. Nocedal, S. J. Wright, Numerical Optimization, 2nd Edition, Springer Series in Operations Research, Springer, New York, 2006.

[56] R. Fletcher, Practical Methods of Optimization, 2nd Edition, John Wiley & Sons, New York, 1987.

[57] D. C. Liu, J. Nocedal, On the limited memory BFGS method for large scale optimization, Math. Program. 45 (1) (1989) 503–528.

[58] COMSOL Multiphysics® v. 6.0. COMSOL AB, Stockholm, Sweden, `https://www.comsol.com` (2022).